

NASA

510-34

N92-14310^{20D} 48266
p. 11

A Navier-Stokes Solution of Hull-Ring Wing-Thruster Interaction

C.-I. Yang (David Taylor Research Center, USA)

P. Hartwich, P. Sundaram, (NASA Langley Research Center, USA)

ABSTRACT

Navier-Stokes simulations of high Reynolds number flow around an axisymmetric body supported in a water tunnel were made. The numerical method is based on a finite-differencing high resolution second-order accurate implicit upwind scheme. Four different configurations were investigated, these are, 1. barebody, 2. body with an operating propeller, 3. body with a ring wing and 4. body with a ring wing and an operating propeller. Pressure and velocity components near the stern region were obtained computationally and are shown to compare favorably with the experimental data. The method correctly predicts the existence and extent of stern flow separation for the barebody and the absence of flow separation for the three other configurations with ring wing and/or propeller.

I. INTRODUCTION

It has been known in marine propulsion technology that certain advantages can be achieved by properly integrating a ring wing and the propeller. With a ring wing that accelerates the flow the efficiency of the propeller remains more or less at a constant level over a wider range of advance ratios. With a ring wing that decelerates the flow, the inception of cavitation on the propeller can be delayed. In order to take advantage of the ring wing to obtain the desirable benefit, a clear understanding of the role it plays is important. Thorough water tunnel experiments and reliable numerical simulations serve as complementary approaches to gain understanding.

By combining the body, ring wing and propeller, appropriate configurations can be generated for water tunnel experiments, and the influence of each individual component can be isolated. The configurations studied here are 1. barebody, 2. body with an operating propeller, 3. body with a ring wing and 4. body with a ring wing and an operating propeller. Data collected from the water tunnel tests included the velocity components around the afterbody and the pressure on the stern. The data show the degree of inter-

action at the given operating conditions and serve as benchmarks for evaluating the present numerical simulations.

One important parameter in hull-propulsor interaction is the thrust deduction coefficient t , which signifies the drag augmentation due to the interaction. In the past, inviscid methods [1,2] have been successful in computing the coefficient t . The methods become somewhat inadequate in a situation where the propulsor unit is imbedded in the stern boundary layer where the viscous effect plays a dominating role. Efforts have been made to address the problem; in particular, Falcão de Campos [3] presented an inviscid approach to calculate the flow on the stern with and without propulsor based on the Euler equation of motion and Huang et al [4] developed a numerical technique to study the interaction between a propeller and unseparated viscous stern boundary layer. To further enhance the ability to predict the effect of hull-propulsor interaction, a Navier-Stokes type viscous analysis is needed. This is particular true when barebody flow separation may occur. Previously, Haussling et al [5] performed extensive numerical simulations of viscous flow about bodies with appendages using a Navier-Stokes solver. Here a three-dimensional incompressible Navier-Stokes solver is used to simulate the flow around a compound propulsor unit on an axisymmetric body supported in a water tunnel with a square cross-section. The solver is based on a high resolution second-order accurate implicit upwind scheme [6,7]. The propeller effect is simulated by imbedding body forces in a disk located at the propeller plane [8,9]. The experimental data were used to validate the Navier-Stokes solver.

II. DESCRIPTION OF EXPERIMENTS

The test body is axisymmetric with a length of 139.12 cm and a maximum diameter of 24 cm. Its radius offsets, y , as a function of axial length, x , are given in cm units by:

```

for 0.00 ≤ x ≤ 24.00
  y = [12.02 - (12.0 - x/2)2]1/2
for 24.00 ≤ x ≤ 97.81
  y = 12
for 97.81 ≤ x ≤ 115.84
  y = [42.672 - (x - 97.81)2]1/2 - 30.67
for 115.84 ≤ x ≤ 129.17
  y = (133.0 - x) tan 25°
for 129.17 ≤ x ≤ 131.93
  y = -0.0214x + 4.554
for 131.93 ≤ x ≤ 139.12
  y = -0.0310x2 + 8.162x - 535.51

```

The ring wing has a NACA 4415 profile section with a 5° angle of attack; its chord length is 5.3 cm. The diameter of ring wing measured at its trailing edge is 16 cm; its trailing edge is located at 129.7 cm from the nose of the body. The propeller has four blades with a diameter of 15.71 cm and was driven from behind with a Z-drive propelling device. The device consists of a tapered forebody, a cylindrical midbody and an elliptical afterbody. The length of the device is about 85 cm and the diameter of midbody is about 10 cm. The propeller plane is located at 135 cm from the nose. The water tunnel in which the experiments were conducted has a square cross-section with round corners and its dimensions are 90 cm × 90 cm. The model/tunnel blockage ratio is about 5.6 percent. The body was supported from the ceiling of the water tunnel with two struts located at x = 14.0 cm and z = 64.0 cm from the nose. A schematic sketch is shown in Fig. 1.; the propeller drive is not included. The geometric tolerances are less than 0.5 mm. The reference length is chosen to be 133.0 cm.

Experiments were conducted at a Reynolds number of 6×10^6 (based on reference length 133.0 cm). The flow measurements were carried out on lines lying on the horizontal plane and perpendicular to the center line. The pressures on the body surface were measured by means of transducers and all signals could be reproduced satisfactorily within 1.0 percent. For the flow measurements, the standard deviation of all signals varied between 0.1 and 2.0 percent.

III. DESCRIPTION OF NUMERICAL PROCEDURE

Using Chorin's artificial compressibility formulation, the incompressible Navier-Stokes equations are written in conservation law form for three-dimensional flow as [10]

$$\mathbf{Q}_t + (\mathbf{E}^* - \mathbf{E}_v^*)_x + (\mathbf{F}^* - \mathbf{F}_v^*)_y + (\mathbf{G}^* - \mathbf{G}_v^*)_z = 0 \quad (1)$$

where the dependent variable vector

$$\mathbf{Q} = (p, u, v, w)^T$$

represents the pressure and velocity components in a Cartesian coordinate system (x, y, z). The inviscid flux vectors \mathbf{E}^* , \mathbf{F}^* , \mathbf{G}^* and the viscous shear flux vectors \mathbf{E}_v^* , \mathbf{F}_v^* , \mathbf{G}_v^* are given by

$$\begin{aligned}
 \mathbf{E}^* &= (\beta u, u^2 + p, uv, uw)^T \\
 \mathbf{F}^* &= (\beta v, uv, v^2 + p, vw)^T \\
 \mathbf{G}^* &= (\beta w, uw, vw, w^2 + p)^T \\
 \mathbf{E}_v^* &= Re^{-1}(0, \tau_{xx}, \tau_{xy}, \tau_{xz})^T \\
 \mathbf{F}_v^* &= Re^{-1}(0, \tau_{yx}, \tau_{yy}, \tau_{yz})^T \\
 \mathbf{G}_v^* &= Re^{-1}(0, \tau_{zx}, \tau_{zy}, \tau_{zz})^T
 \end{aligned} \quad (2)$$

The coordinates x, y, z are scaled with an appropriate characteristic length scale L. The velocity components u, v, w are nondimensionalized with respect to the free stream velocity V_∞ , while the normalized pressure is defined as $p = (P - P_\infty)/\rho V_\infty^2$. The kinematic viscosity ν is assumed to be constant, and the Reynolds number is defined as $Re = \frac{V_\infty L}{\nu}$. The artificial compressibility parameter β monitors the error associated with the addition of the unsteady pressure term $\frac{\partial p}{\partial t}$ in the continuity equation which is needed for coupling the mass and momentum equations in order to make the system hyperbolic.

Equations (1) can be transferred to a curvilinear, body-fitted coordinates system (ζ , ξ and η) through a coordinate transformation of the form

$$\zeta = \zeta(x, y, z), \quad \xi = \xi(x, y, z) \quad \text{and} \quad \eta = \eta(x, y, z)$$

Eq. (1) becomes

$$(\mathbf{Q}/\mathbf{J})_t + (\mathbf{E} - \mathbf{E}_v)\zeta + (\mathbf{F} - \mathbf{F}_v)\xi + (\mathbf{G} - \mathbf{G}_v)\eta = 0 \quad (3)$$

with

$$(\mathbf{E}, \mathbf{F}, \mathbf{G})^T = [\mathbf{T}] \quad (\mathbf{E}^*, \mathbf{F}^*, \mathbf{G}^*)^T$$

and

$$(\mathbf{E}, \mathbf{F}, \mathbf{G})^T = [\mathbf{T}] \quad (\mathbf{E}_v^*, \mathbf{F}_v^*, \mathbf{G}_v^*)^T$$

, where

$$[\mathbf{T}] = \begin{bmatrix} \zeta_x & \zeta_y & \zeta_z \\ \xi_x & \xi_y & \xi_z \\ \eta_x & \eta_y & \eta_z \end{bmatrix}$$

and the Jacobian of the coordinate transformation is given by

$$J^{-1} = \det \begin{bmatrix} x_\zeta & y_\zeta & z_\zeta \\ x_\xi & y_\xi & z_\xi \\ x_\eta & y_\eta & z_\eta \end{bmatrix}$$

The Cartesian derivatives of the shear fluxes are obtained by expanding them using chain rule expansions in the ζ , ξ , and η directions.

Defining computational cells with their centroids at $l = \frac{\theta}{\Delta\theta}$ (θ is ζ , ξ , or η) and their cell interfaces at $l \pm 1/2$, the backward Euler time differencing of the three-dimensional conservation form is

$$\frac{\Delta \mathbf{Q}^n}{\Delta t} = -[\Delta_\zeta(\mathbf{E}^{n+1} - \mathbf{E}_v^{n+1}) + \Delta_\xi(\mathbf{F}^{n+1} - \mathbf{F}_v^{n+1}) + \Delta_\eta(\mathbf{G}^{n+1} - \mathbf{G}_v^{n+1})] \quad (3)$$

where Δt is the time step, $\Delta \mathbf{Q}^n = \mathbf{Q}^{n+1} - \mathbf{Q}^n$ and $\Delta_l(\cdot) = [(\cdot)_{l+1/2} - (\cdot)_{l-1/2}] / \Delta\theta$. Superscript denotes the time level at which the variables are evaluated.

Linearizing Eq. (3) about time level n , we obtain

$$\begin{aligned} & [\frac{\mathbf{I}}{\Delta t J} + (\frac{\partial \mathbf{E}^n}{\partial \mathbf{Q}} - \frac{\partial \mathbf{E}_v^n}{\partial \mathbf{Q}}) \Delta_\zeta + (\frac{\partial \mathbf{F}^n}{\partial \mathbf{Q}} - \frac{\partial \mathbf{F}_v^n}{\partial \mathbf{Q}}) \Delta_\xi \\ & + (\frac{\partial \mathbf{G}^n}{\partial \mathbf{Q}} - \frac{\partial \mathbf{G}_v^n}{\partial \mathbf{Q}}) \Delta_\eta] \Delta \mathbf{Q}^n \\ & = -[\Delta_\zeta(\mathbf{E}^n - \mathbf{E}_v^n) + \Delta_\xi(\mathbf{F}^n - \mathbf{F}_v^n) + \Delta_\eta(\mathbf{G}^n - \mathbf{G}_v^n)] \end{aligned} \quad (4)$$

where \mathbf{I} is the identity matrix.

The left hand side is the implicit part and the right hand side is the explicit part of the formulation. The explicit part is the spatial derivatives in Eq. 2 evaluated at the known time level n ; its value diminishes as the steady state solution is approached. Hence, it is also called the residual. The L_2 norm of the residual is often used as a measure of convergence of a solution. Letting the flux Jacobians \mathbf{A} , \mathbf{B} and \mathbf{C} be defined as follow

$$\mathbf{A} \equiv \frac{\partial \mathbf{E}^n}{\partial \mathbf{Q}}, \quad \mathbf{B} \equiv \frac{\partial \mathbf{F}^n}{\partial \mathbf{Q}}, \quad \mathbf{C} \equiv \frac{\partial \mathbf{G}^n}{\partial \mathbf{Q}},$$

discretize the inviscid and viscous fluxes according to upwind differencing scheme and central differencing scheme respectively in ζ , ξ and η coordinate direction independently and then assemble them together. Equation (4) becomes

$$\begin{aligned} & [\frac{\mathbf{I}}{\Delta t J}] \\ & -(\mathbf{A}^- + \mathbf{X})_{i+\frac{1}{2}} \Delta_{i+\frac{1}{2}} + (\mathbf{A}^+ + \mathbf{X})_{i-\frac{1}{2}} \Delta_{i-\frac{1}{2}} \\ & -(\mathbf{B}^- + \mathbf{Y})_{j+\frac{1}{2}} \Delta_{j+\frac{1}{2}} + (\mathbf{B}^+ + \mathbf{Y})_{j-\frac{1}{2}} \Delta_{j-\frac{1}{2}} \\ & -(\mathbf{C}^- + \mathbf{Z})_{k+\frac{1}{2}} \Delta_{k+\frac{1}{2}} + (\mathbf{C}^+ + \mathbf{Z})_{k-\frac{1}{2}} \Delta_{k-\frac{1}{2}}]^n \Delta \mathbf{Q}^n \\ & = -RES(\mathbf{Q}^n) \end{aligned} \quad (5)$$

where i , j , and k are spatial indices associated with the ξ , η and ζ coordinate direction. \mathbf{A}^\pm , \mathbf{B}^\pm and \mathbf{C}^\pm are flux matrices split from the flux Jacobians \mathbf{A} , \mathbf{B} and \mathbf{C} according to the signs of their eigenvalues. The residual $RES(\mathbf{Q}^n)$ is evaluated with a TVD technique together with Roe's [11] flux-difference splitting scheme, the discretization is third-order accurate. Conventional second-order central differencing is applied to obtain the viscous flux matrices \mathbf{X} , \mathbf{Y} and \mathbf{Z} . Equation(5) is solved by an implicit hybrid algorithm, where a symmetric planar Gauss-Seidel relax-

ation is used in the streamwise direction ζ in combination with approximate factorization in the remaining two coordinate directions ξ and η . It is used to avoid the Δt^3 spatial splitting error incurred in fully three-dimensional approximate factorization methods. This scheme is unconditionally stable for linear systems and offers the advantage of being completely vectorizable like a conventional three-dimensional approximate factorization algorithm. As a result, Eq. (5) becomes

$$\begin{aligned} & [\mathbf{M} - (\mathbf{B}^- + \mathbf{Y})_{j+\frac{1}{2}} \Delta_{j+\frac{1}{2}} + (\mathbf{B}^+ + \mathbf{Y})_{j-\frac{1}{2}} \Delta_{j-\frac{1}{2}}] \Delta \hat{\mathbf{Q}} \\ & = -RES(\mathbf{Q}^n, \mathbf{Q}^{n+1}) \\ & [\mathbf{M} - (\mathbf{C}^- + \mathbf{Z})_{k+\frac{1}{2}} \Delta_{k+\frac{1}{2}} + (\mathbf{C}^+ + \mathbf{Z})_{k-\frac{1}{2}} \Delta_{k-\frac{1}{2}}] \Delta \mathbf{Q}^n \\ & = \mathbf{M} \Delta \hat{\mathbf{Q}} \\ & \mathbf{Q}^{n+1} = \mathbf{Q}^n + \Delta \mathbf{Q}^n \end{aligned} \quad (6)$$

with

$$\mathbf{M} = [\frac{\mathbf{I}}{\Delta t J} + (\mathbf{A}^- + \mathbf{X})_{i+\frac{1}{2}} + (\mathbf{A}^+ + \mathbf{X})_{i-\frac{1}{2}}],$$

and the residual on the RHS indicates the nonlinear updating of the residual by using \mathbf{Q}^{n+1} whenever it becomes available while sweeping in the ζ direction back and forth through the computational domain.

For laminar flow computations the coefficient of molecular viscosity $\mu = \mu_l$ is obtained from Sutherland's law. Turbulence is simulated using the Baldwin-Lomax algebraic turbulence model[12]. For turbulent flow laminar viscosity coefficients are replaced by

$$\mu = \mu_l + \mu_t$$

The turbulent viscosity coefficient μ_t is computed by using the isotropic, two-layer Cebeci type algebraic eddy-viscosity model as reported by Baldwin-Lomax. Modifications proposed by Degani and Schiff [13] and Hartwich and Hull [14] were implemented.

IV. DESCRIPTION OF BODY FORCE PROPELLER MODEL

The principle of the body force model is to introduce the body force terms into the Navier-Stokes equation to include the effects of the propeller. The essential parameters that define the propeller effects are the thrust coefficient C_T , the torque coefficient C_Q , the advance coefficient J and the radial circulation distribution $G(r)$. The same parameters were used to define the body force for the propeller model. The thrust and torque coefficients are defined as follow:

$$C_T = \frac{T}{\frac{1}{2} \rho V^2 \frac{\pi}{4} D^2}, \quad C_Q = \frac{Q}{\frac{1}{2} \rho V^2 \frac{\pi}{4} D^3}$$

where T and Q are thrust and torque, respectively. D is the diameter of the propeller. The axial and circumferential body force per unit volume are obtained from

the following equations:

$$fb_x = \frac{C_T P_p^2 G(r)}{4\Delta X \int_{R_h}^{R_p} G(r) r dr}$$

$$fb_\theta = \frac{C_Q R_p^3 G(r)}{2r \Delta X \int_{R_h}^{R_p} G(r) r dr}$$

where fb_x and fb_θ are the body forces per unit volume in the axial and circumferential directions, respectively, R_h and R_p are the radii of propeller hub and blade tip, respectively, and ΔX is the thickness of the disk. The computed body forces are then incorporated into the right hand side of Eq. 5 and form a part of the residual. Only a slight modification to the flow solver is needed to accommodate the body force type propeller model and there is no need for special gridding.

In reality, the blade circulation distribution $G(r)$ depends upon the inflow at the propeller plane which in turn is influenced by the blade circulation. This mutual dependency implies that the body forces fb_x and fb_θ which are functions of $G(r)$ should be obtained by an iterative procedure. To complete this procedure, knowledge of propeller-induced axial and tangential velocities, u_a and u_t is needed. A propeller program based on the vortex-lattice lifting-surface method developed by Greeley and Kerwin [15] can be used for this purpose. The iterative procedure can be described as follow:

1. Calculate the nominal inflow with the Navier-Stokes solver.
2. Obtain the circulation distribution $G(r)$, the induced-velocities u_a and u_t , the thrust and torque coefficients C_T and C_Q by using the calculated nominal inflow as input to the propeller program [15].
3. Compute the body forces fb_x and fb_θ by using the calculated circulation distribution $G(r)$, thrust and torque coefficients C_T and C_Q .
4. Obtain the total velocities at the propeller plane by using the Navier-Stokes solver with the information obtained in step 3.
5. Compute the effective wake by subtracting the propeller-induced velocities obtained in step 2 from the total velocities obtained in step 4.
6. Obtain an updated circulation distribution, propeller-induced velocities, and thrust and torque coefficients by using the newly computed effective wake as input to the propeller program.
7. Repeat the process from step 1 to step 6 until the total velocities, the body forces and the propeller-induced velocities are unchanged.

It has been shown that this procedure converged after two iterations [8]. For the purpose of illustration, the results presented in following are obtained by using measured thrust and torque without any iteration. In spite of its simplicity, it was able to predict the flow

pattern around the propeller disk and the stern region rather accurately [8,9].

V. GRID GENERATION

Based on the configuration shown in Fig. 1, which models the experimental setup described in Section II above, a 180° sector of the tunnel needs to be modelled in order to resolve the effect on flow due to the supporting struts. This requires a large amount of grid points and extensive computational resources. After one computation for the barebody configuration, it was found that the struts produced an influence around and directly behind them with no significant effect on the horizontal plane on which measurements were made. Therefore, the struts were eliminated allowing the numerical simulations to be performed accurately in a 90° sector of the tunnel. Also included, due to its proximity to the stern, is the propeller drive.

To include the ring wing geometry, two block $C-O$ type grids were generated. The grid points were matched at the branch cut that separated the two blocks. Computations were performed on a CRAY-YMP machine which has eight processors. Computational efforts on the two blocks can be performed on two processors simultaneously. For the purpose of synchronization between the processors, it is more efficient if the number of computations is the same for each block. For this reason, each block has the same number of grid points. The grid system was generated by a transfinite interpolation technique. Several grid systems with different number of grid and distributions had been generated and were used for computations on barebody configuration in order to investigate the relationship between the convergence and grid density and distribution. The grid systems examined include 1. a two block $25 \times 49 \times 110$ (r, θ, x) grids, 2. a two block $25 \times 25 \times 90$ grids and 3. a two block $25 \times 13 \times 98$ grids. Grid points were clustered near the boundaries such as tunnel wall and body and ring wing surfaces where the viscous effect dominates. The minimum spacing normal to the body surface for the three grid systems mentioned above is 5.0×10^{-4} . The differences between the solutions based on the grid system 1 and 3 are about two percent which is within the reported experimental accuracy. The results presented below are based on a two block $25 \times 13 \times 98$ (r, θ, x) coarse grid system. Convergence is achieved when the L_2 normal of all residuals is reduced by three order of magnitude with $CFL=10$. Computational CPU time is 40 μ sec per node per iteration. For each computation, over 500 iterations were carried out to ensure convergence.

VI. BOUNDARY CONDITIONS

On the solid boundaries such as surfaces of tunnel wall, ring wing, body and propeller drive the no-slip condition is applied, in addition, the normal gradient

of the pressure is assumed to be zero. Freestream condition is applied as inflow condition. Zero-order extrapolation is used to obtain the outflow conditions.

During the computation process, the variables on the branch cut that separates the two blocks are not computated. At the end of each iteration, these variables are updated by averaging the values at the adjacent grid points from each block. The averaging process is linear. The updated values are then used as boundary conditions for both blocks for the next iteration.

VII. RESULTS AND DISCUSSIONS

The four configurations that were investigated are 1. flow over the barebody, 2. flow over the body with an operating propeller, 3. flow over the body with a ring wing and 4. flow over the body with a ring wing and an operating propeller. Computational results are presented in the form of velocity profiles and pressure contours in the stern region; they are compared with available experimental data. In addition, to facilitate the flow visualization and discussion, computed particle trace are also included. The length scale was normalized with reference length $L = 133\text{cm}$.

Case 1. Flow over the Barebody

In this test case, the configuration is simple but the flow is rather interesting. At a Reynolds number of 6.0×10^6 , flow separation was observed in the stern region. Figure 2 shows the velocity vectors in the stern region from both computation and experiment. The correlation is good except at the axial location $X/L = 0.89$ where the experiment shows a somewhat fuller profile near the body. Figure 3 shows the particle traces and clearly depicts the separation bubble. The predicted separation location is about 1.5 cm (1.13 percent of body length) ahead of where it was observed experimentally. Figure 3 also indicates that the size of the bubble is predicted correctly. Figure 4 shows the predicted and measured pressure distributions on the surface of the stern. The surface pressure begins to recover as the flow passes the shoulder of the afterbody at $X/L = 0.78$. The recovery levels off where flow separation takes place. Figure 5 shows the pressure contours in the stern region.

Case 2. Flow over the Body with an Operating Propeller

In this test case, the propeller was operating at $J = 0.47$ and $V = 4\text{m/s}$; C_T and C_Q were measured as 2.052 and 0.247, respectively. To apply the body force propeller model, the circulation $G(r)$ was assumed to be distributed over the disk according to:

$$G(r) = r(1 - r)^{1/2}$$

with $r = (y - y_{hub})/(R_p - y_{hub})$. The propeller was located at $X/L = 1.015$.

Figure 6 shows the comparison of predicted and measured velocity vectors in the stern region. The prediction confirms that the separation bubble is removed due to the propeller suction. Experimental data indicate stronger downward radial velocities at all four stations. In addition, at axial locations $X/L = 0.89$ and $X/L = 0.93$ the predicted velocity profiles are less full than those that were measured near the body. It is found from computations that the predictions behind the propeller are sensitive to the circulation distribution over the propeller disk and the axial locations at which the predictions are made. Figure 7 shows the particle traces, indicating that flow contraction takes place immediately in front of and behind the propeller disk. Figure 8 shows the predicted and measured pressure distributions on the surface of the stern. The difference between the pressures presented in Fig. 8 and Fig. 4 gives the amount of the pressure drag on the barebody due to propeller action. The added drag constitutes the major part of the thrust deduction fraction (t). The agreement between prediction and measurement is very good. This is an indication that thrust deduction $(1 - t)$ can be predicted correctly with this numerical method. Figure 9 shows the pressure contours in the stern region; the pressure jump across the propeller plane is clear.

Case 3. Flow over the Body with a Ring Wing

An intended function of the ring wing was to accelerate the flow and produce thrust. It was also expected that the flow separation over the stern would be removed once the ring wing was in place. Figure 10 shows the velocity vectors in the stern region from both computation and experiment. In comparison with Fig. 2, it can be seen that the ring wing achieved its function in accelerating the flow and removing the stern separation. The predicted and the measured velocity vectors are in good agreement. Due to lack of details, the experimental data failed to resolve the wake structure behind the ring wing. Figure 11 shows the particle traces and there is no detectable flow separation on the surface of either the body or the ring wing. Figure 12 shows the pressure on the stern surface. Note that the predicted surface pressure immediately upstream of the ring wing's leading edge at $X/L = 0.93$ is somewhat higher than that measured. Figure 13 shows the pressure contours in the stern region. Clearly shown are the locations of the pressure and suction peaks on the ring wing surface.

Case 4. Flow over the Body with a Ring Wing and an Operating Propeller

In this test case, the propeller was operating at $J = 0.47$ and $V = 4m/s$; C_T and C_Q were measured as 2.081 and 0.250, respectively, and are about 2 percent higher than those shown in Case 2. Figure 14 shows the comparison of predicted and measured velocity vectors in the stern region. The agreement is quite good. Figure 15 shows the particle traces. It can be seen that flow is accelerated as it passes the ring wing and is contracted as it passes the propeller disk. Figure 16 shows the pressure on the stern surface. The discrepancy between the predicted and measured pressure immediately upstream of the ring wing at $X/L = 0.93$ as discussed in Case 3 is present here also. The difference between the pressures presented in Fig. 16 and Fig. 12 gives the amount of the pressure drag on the body due to the propeller action, the agreement between the prediction and measurement is very good, despite the discrepancy mentioned above. Figure 17 shows the pressure contours in the stern region.

VIII. CONCLUSION

A numerical method based on a finite-differencing high resolution second-order accurate implicit upwind scheme was used to discretize the three-dimensional Navier-Stokes equations. Simulations of flow over an axisymmetric body with a compound propulsor supported in a square water tunnel were performed. A body force type propeller model was used to simulate the propeller action. Results indicate that this numerical method is effective and accurate. Observed flow phenomena such as separation, acceleration and contraction were realistically predicted. The pressure drags due to propeller action were computed correctly. A ring wing may affect the circulation distribution on the propeller, depending on its proximity to the propeller. In order to improve the predictions further, an iterative procedure described in section IV will be explored in a future study.

ACKNOWLEDGEMENT

This study was supported by The Office of Naval Technology under David Taylor Research Center Work Unit 1-1506-060-40. The computing time of CRAY-YMP was provided generously by NASA Ames Numerical Aerodynamic Simulation (NAS) Program. The experimental data presented in this paper are of foreign origin, obtained via informal correspondance.

REFERENCES

1. Wald, Q., "Performance of a Propeller in a Wake and the Interaction of Propeller nad Hull", Journal of Ship Research, Vol 9, no. 1, Jun. 1965, pp1-8.
2. Beveridge, J.L., "Analytical Prediction of Thrust Deduction for Submersibles and Surface Ships", Journal of Ship Research, Vol. 13, no. 4, Dec. 1969, pp. 258-271
3. Falcão de Campos, J.A.C., "On the Calculation of Ducted Propeller Performance in Axisymmetric Flows", Technical Report 696, Netherlands Ship Model Basin, Wageningen, The Netherlands, 1983
4. Huang, T. T., Wang, H. T., Santelli, N., Groves, N. C., "Propeller/Stern/Boundary Layer Interaction on Axisymmetric Bodies, Theory and Experiment", DTRC Report 76-0113, 1976.
5. Haussling, H.J., Gorski, J.J., Coleman, R., "Computation of Incompressible Fluid Flow about Bodies with Appendages", Presented at International Seminar on Supercomputing in Fluid Flow, Lowell, Massachusetts, 3-5 Oct. 1989.
6. Hartwich, P.-M., Hsu, C. H., "High Resolution Upwind Schemes for the Three-Dimensional, Incompressible Navier-Stokes Equations", AIAA Journal, Vol. 26, No. 11, Nov. 1988, pp 1321-1328.
7. Hartwich, P.-M., Hsu, C. H. and Liu, C.H., "Vectorizable Implicit Algorithms for the Flux-Difference Split, Three-Dimensional, Incompressible Navier-Stokes Equations", ASME Journal of Fluids Engineering, Vol. 110, No. 3, Sept. 1988, pp 297-305.
8. Stern, F., Kim, H.T., Patel, V.C., Chen, H.C., "A Viscous Flow Approach to the Computation of Propeller-Hull Interaction", Journal of Ship Research, Vol.32, No. 4, Dec. 1988, pp 246-262.
9. Yang, C-I, Hartwich, P.-M., Sundaram, P., "Numerical Simulation of Three- Dimensional Viscous Flow around a Submersible Body", The Proceedings Fifth International Conference on Numerical Ship Hydrodynamics, Sept. 25-28 1989, Hiroshima, Japan.
10. Chorin, A. J., "A Numerical Method for Solving Incompressible Viscous Flow Problems", Journal of Computational Physics, Vol. 2, No. 1, Aug. 1967, pp 12-26.
11. Roe, P.L., "Approximate Riemann Solvers, Parameter Vectors, and Difference Schemes", Journal of Computational Physics, Vol. 43, No. 2, Oct. 1981, pp 357-372.

12. Baldwin, B.S., Lomax, H., "Thin Layer Approximation and Algebraic Model for Separated Turbulent Flows", AIAA Paper 78-257 Jan. 1978.
13. Degani, D., Schiff, L.B., "Computation of Turbulent Supersonic Flows around Pointed Bodies Having Crossflow Separation", Journal of Computational Physics, Vol. 66, No. 1, Sept. 1986, pp 173-196.
14. Hartwich, P-M., Hall R.M., "Navier-Stokes Solutions for Vortical Flows over a Tangent-Ogive Cylinder", AIAA Paper No. 89-0337, Jan. 1989
15. Greeley, D.S., Kerwin, J.E., "Numerical Methods for Propeller Design and Analysis in Steady Flow", Trans. SNAME, Vol. 90, 1982, pp. 415-453.

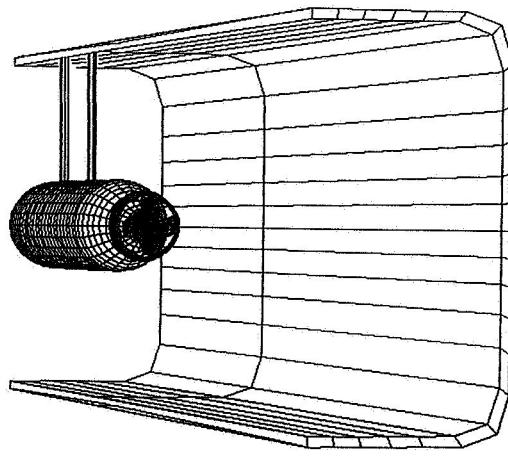


Figure 1. Schematic Sketch of Test Configuration

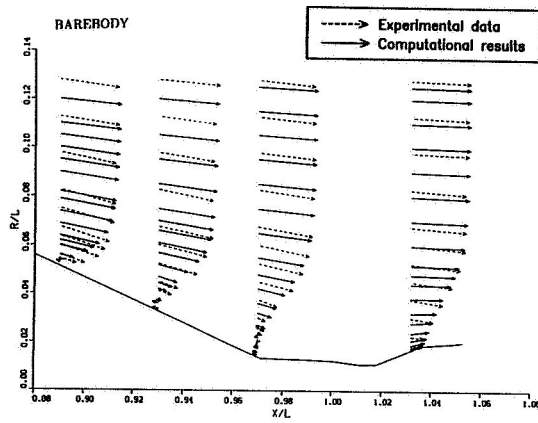


Figure 2. Velocity Vectors in Stern Region for Case 1

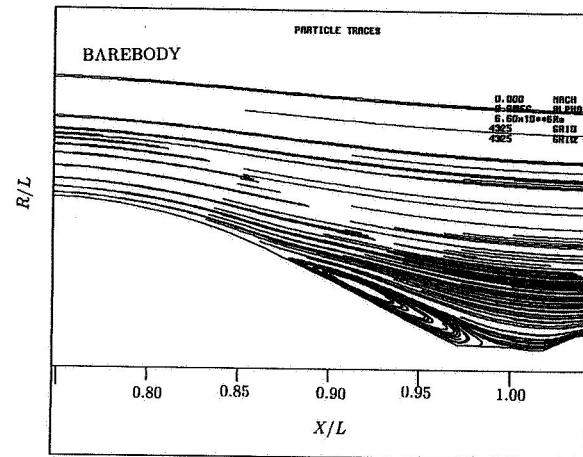


Figure 3. Particle Traces for Case 1

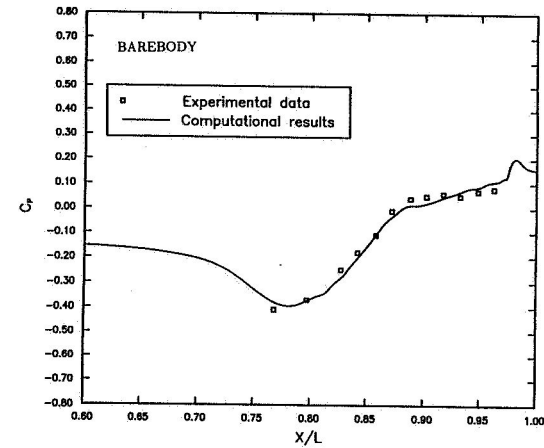


Figure 4. Pressure Distribution on Stern Surface for Case 1

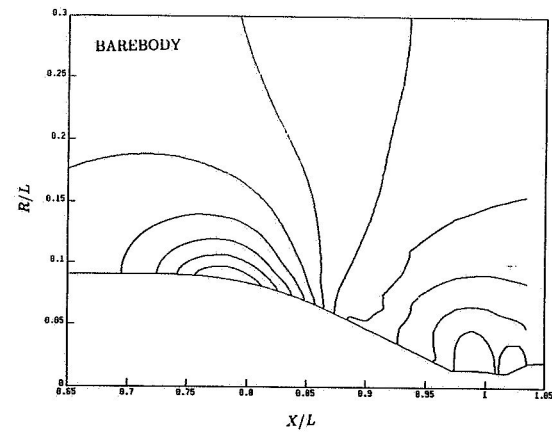


Figure 5. Pressure contours in Stern Region for Case 1

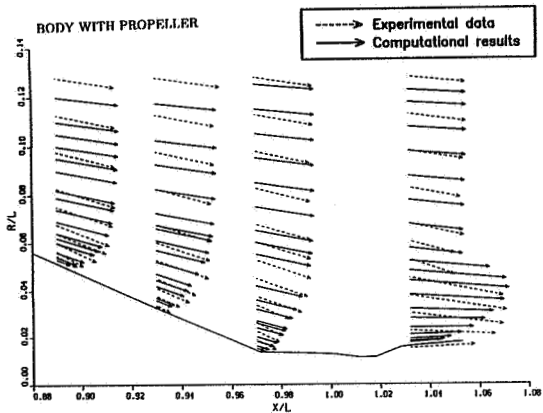


Figure 6. Velocity Vectors in Stern Region for Case 2

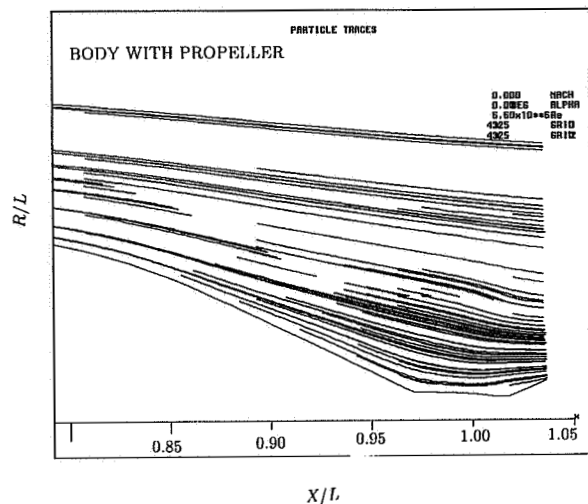


Figure 7. Particle Traces for Case 2

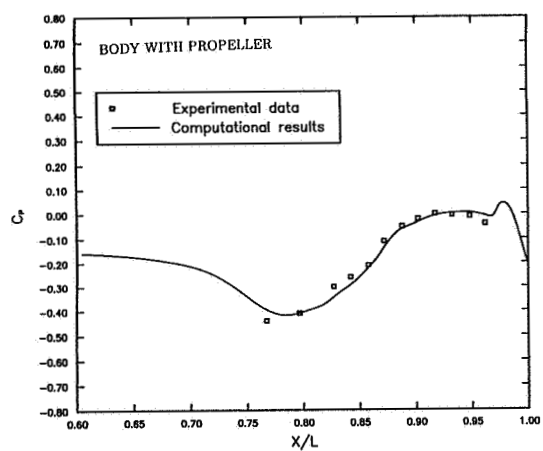


Figure 8. Pressure Distribution on Stern Surface for Case 2

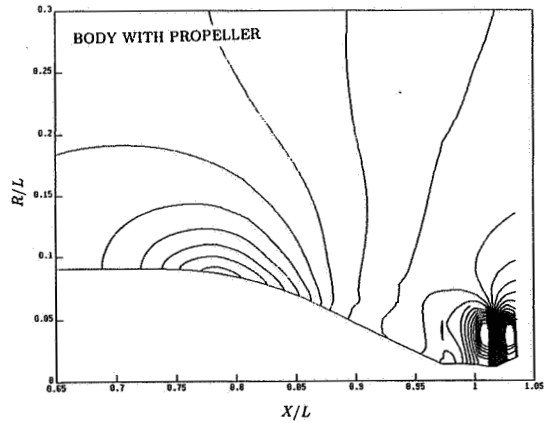


Figure 9. Pressure contours in Stern Region for Case 2

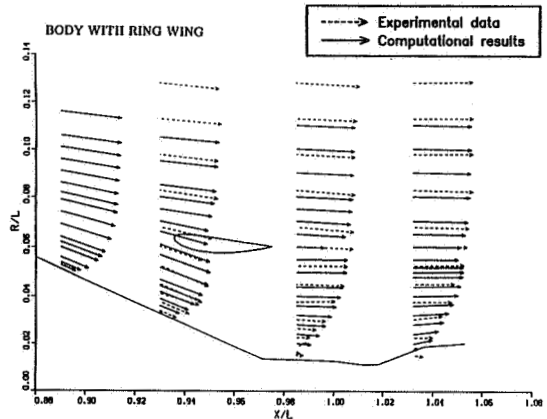


Figure 10. Velocity Vectors in Stern Region
for Case 3

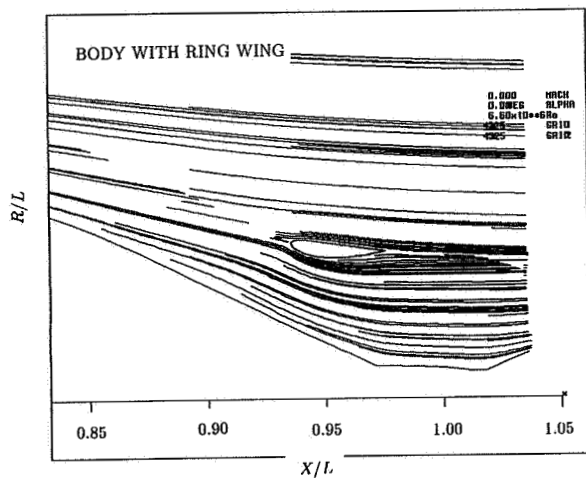


Figure 11. Particle Traces for Case 3

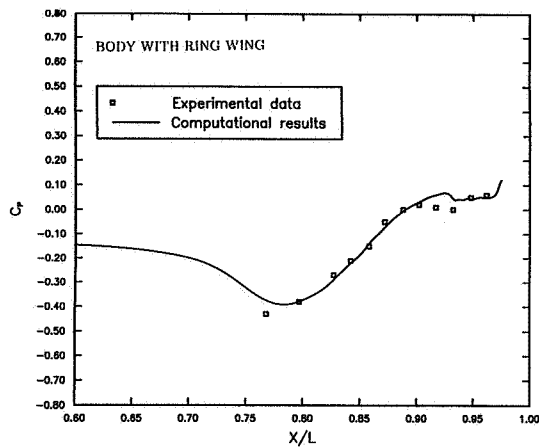


Figure 12. Pressure Distribution on Stern Surface for Case 3

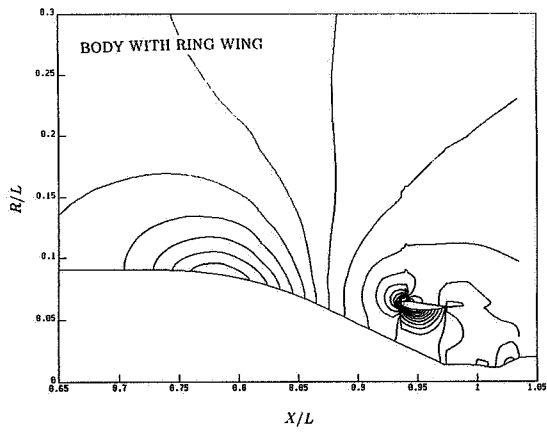


Figure 13. Pressure contours in Stern Region for Case 3

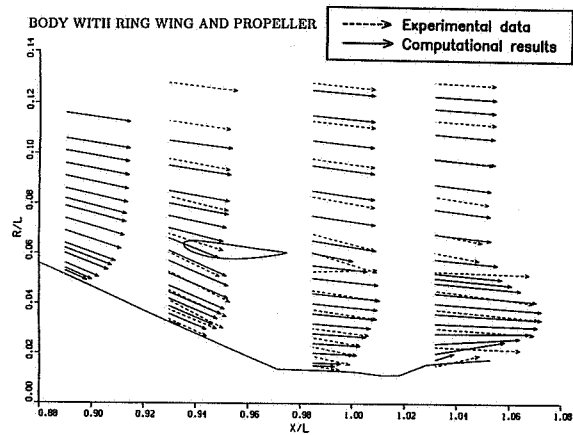


Figure 14. Velocity Vectors at Stern Region for Case 4

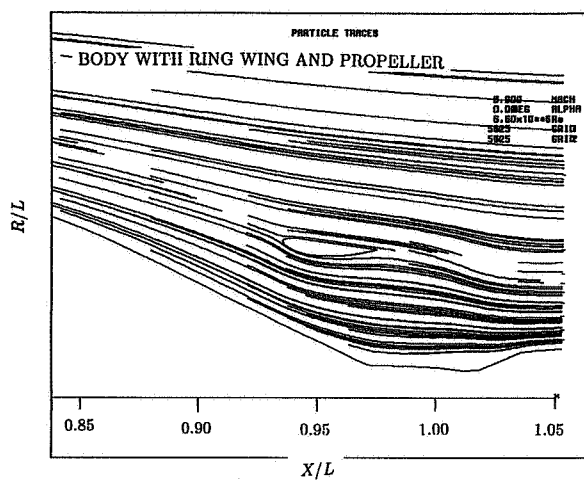


Figure 15. Particle Traces for Case 4

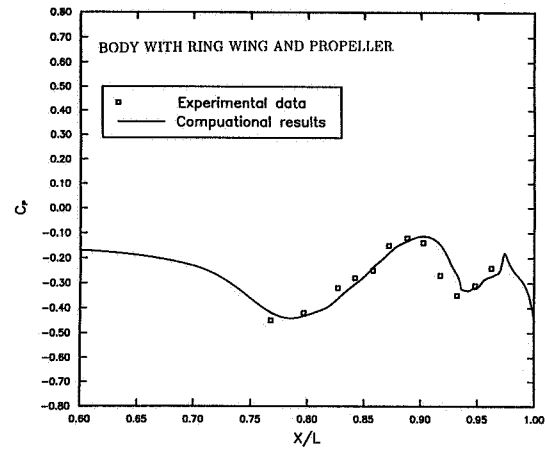


Figure 16. Pressure Distribution on Stern Surface for Case 4

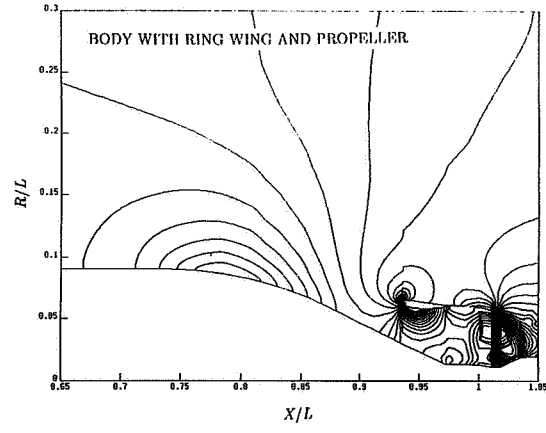


Figure 17. Pressure contours in Stern Region for Case 4

DISCUSSION

Philippe Genoux
Bassin d'Essais des Carènes, France

It is well known that Navier Stokes solvers may have difficulties at high Reynolds numbers. How does your code behave at full scale Reynolds numbers?

AUTHORS' REPLY

The differencing scheme presented in this paper is based on hyperbolic formulation, assuming that at high Reynolds numbers the behavior of Navier-Stokes equations becomes hyperbolic-like. At present, the solver has been used to simulate flow at Reynolds number 15×10^6 . The agreement between computation and experiment is good. No convergence problem was experienced.

DISCUSSION

Fred Stern
The University of Iowa, USA

The results presented display some interesting features for a ducted propulsor; however, it would be of greater interest if the authors would include the propulsor-hull interaction, i.e., make full use of the viscous-flow approach to propulsor-hull interaction and demonstrated in Reference [8].

AUTHORS' REPLY

We appreciate Prof. Stern's comments and suggestions. We are using the method described in Reference [8] for our future work.